nature communications

Article

https://doi.org/10.1038/s41467-025-65749-1

Accurate geometric albedo, shape, and size of Hi'iaka from a stellar occultation

Received: 17 July 2024

Accepted: 21 October 2025

Published online: 01 December 2025

Check for updates

A list of authors and their affiliations appears at the end of the paper

Stellar occultations, when a distant object passes in front of a star and casts a shadow on Earth, are a powerful tool to probe the physical properties of solar system bodies. They enable precise size and shape measurements and can reveal rings, satellites, atmospheres, or surface features. Here we present results from two stellar occultations by Hi'iaka, dwarf planet Haumea's largest satellite, observed in April 2021. The second event yielded the first documented multi-chord occultation involving a trans-Neptunian satellite other than Charon. Combining these data with photometric observations, we find that Hi'iaka is a triaxial ellipsoid with a volume-equivalent diameter of 370 ± 20 km and a density of 640 ± 80 kg/m^3, indicating a porous interior. The visible geometric albedo is 0.76 ± 0.15, (~30% higher than Haumea's). The combination of low density and rapid rotation (9.68 ± 0.02 hours), under the assumption of a homogeneous body, indicates that Hi'iaka deviates from hydrostatic equilibrium.

Hi'iaka is the largest satellite of the trans-Neptunian object (TNO) and dwarf planet Haumea[1], which orbits the Sun at an average distance of approximately 43 au with an orbital inclination of around 28°. Some aspects of the Haumea system lead to the expectation that Hi'iaka should be in a synchronous orbit, i.e., that its rotational and orbital periods are equivalent. Specifically, one of the favored formation scenarios of the system is a non-catastrophic graze-and-merge collision[2,3] that produced Hi'iaka, and Haumea's other satellite Namaka, close to Haumea, with subsequent outward migration of the satellites onto synchronous orbits. This formation theory is consistent with the nearly circular orbit of Hi'iaka[4], the presence of two satellites, and the existence of a ring system[5]. However, Hi'iaka's semi-major axis is nearly 50,000 km and it takes approximately 49 days to complete an orbit around Haumea[4], but needs only around 9.8 h to complete one full rotation[6]. These factors combine for a synchronization time longer than the age of the solar system, which is typically associated with the capture formation scenario. On the other hand, Hi'iaka's spectrum presents strong water ice absorption features very similar to those in the spectra of Haumea and the other collisional family members[7,8], strongly indicating that Hi'iaka formed from Haumea's mantle. While much is known about Hi'iaka's orbit and the Haumea system, more information is required about the physical properties of Hi'iaka itself in order to better constrain the formation mechanisms.

Aside from spacecraft visits, stellar occul-tations are perhaps the most powerful method to obtain high-precision constraints on a body's physical properties, including the diameter, shape, albedo, and density (when combined with reasonable mass estimates). A stellar occultation occurs when a solar system body passes in front of a background star, making the star disappear and resulting in a shadow path from which the shape and dimensions of the object can be reconstructed. Detecting one of these events for a trans-Neptunian object can be difficult because these objects' orbits usually present larger uncertainties than their angular diameters. Furthermore, when predicting a stellar occultation by a satellite, the uncertainty on the predicted position of the object includes both the TNO's orbital uncertainty and the uncertainty of the satellite's orbit around the primary. Therefore, predicting a stellar occultation by a TNO satellite is extremely challenging and was first successfully demonstrated for Hi'iaka in 2021. All other (non-Charon) satellites studied via stellar occultations published so far have been serendipitous detections (e.g[9],). The detection of these two stellar occultations by Hi'iaka represents an inflection point in the use of this technique.

In this work, we analyze the results from the two stellar occultations produced by Hi'iaka and extract its physical properties. We place these properties in the context of the formation scenarios that have

e-mail: estela@ucf.edu; ortiz@iaa.edu

been proposed so far to understand the origins of Hi'iaka, the Haumea system, and the Haumea family.

Results

On April 6th and 16th, 2021, Hi'iaka occulted the stars Gaia EDR3 1229416731870211200 (or UCAC4 531-055227) and Gaia ER3 1229336188348183808 (or UCAC4 531- 055209), with Gaia *G*-band magnitudes of 12.6 and 12.4, respectively (see Table 1 for detailed information on the occulted stars). For April 6th, a total of 15 telescopes located in Spain, Morocco, and Algeria attempted to observe the stellar occultation. Only one positive detection was obtained in this campaign with the TRAPPIST-North telescope in Oukaïmeden (Morocco[10]). On April 16th, a large campaign involving telescopes all over the continental United States and southern Canada, including the Research and Education Collaborative Occultation Network (RECON) and the International Occultation Timing Association (IOTA), was carried out. A total of 30 telescopes attempted to observe this stellar occultation, resulting in five positive detections (plus one visual non-recorded detection not included in the analysis). The locations of the observatories can be seen in Fig. 1.

The specifications of the observations are provided in the Methods section, under the subsection Stellar Occultations: Observations and Results, along with the photometric procedures applied to the images. We obtained a unique light curve from each of the telescopes that reported observations. The normalized positive light curves (those where the star disappears, also known as chords) can be seen in Fig. 2, where offsets to the relative flux have been added for clarity. From each chord, we extract the moment in which the star disappears and reappears, otherwise known as the ingress and egress times. The results are presented in Table 2, together with the duration of the occultation in seconds.

The occultation times with their 1-σ uncertainties are translated to a bi-dimensional frame (f,g) with origin on the object's position as given by its ephemeris at the instant of the closest approach (see Fig. 3). In this work, we used the Hi'iaka ephemeris from the Miriade service combined with the Haumea ephemeris from JPL (orbit ID #110).

The methodology used in this work consists of creating a large set of 3D triaxial shape models with a homogeneous surface brightness and random values for the a, b, and c true semi-axes (where $a > b > c$) using the equations provided by[11]. We also made use of the known rotational light curve from[6], new observations to obtain the rotational phase at which the stellar occultations occurred (see Method Section, subsection Hi'iaka's Rotational Light Curve Observations and Results), and Haumea's aspect angle.

The resulting triaxial ellipsoid has semi-axes $a = 240 \pm 40$, $b = 180 \pm 30$, and $c = 143 \pm 7$ km, with an aspect angle of $\theta = 68^\circ \pm 3^\circ$, which is in agreement with the aspect angle of Haumea (assumed to be that of the ring). This value was calculated to be $\theta = 76.2^\circ \pm 0.5^\circ$ in 2017 and it has decreased since then by no more than 5 degrees[5]. Our result is also in agreement (within the 2-σ level) with the aspect angle provided by the pole orientation given in[12] for Haumea, $71.1^{0.6}_{-0.7}$ deg, at the time of the occultation, confirming the idea of the rings being near the equatorial plane. On April 16th, the position angle of Hi'iaka's limb was 112° ± 3° (Table 3). Since the occultation occurred near a maximum in the rotational light curve (see Section Methods, Subsection Rotational Light Curve Results), this angle should closely match the projected orientation of Hi'iaka's spin axis. This means that Hi'iaka's spin axis is aligned with that of Haumea within the error bars. The projected shapes fitted to the correspoding chords for each occultation are shown as black lines in Fig. 3.

The ellipsoidal fit provides a rotationally averaged area-equivalent diameter of 360 ± 30 km for April 16th. To obtain the geometric albedo in V-band, p_V, we used the equation:

$$D = C p_V^{-1/2} 10^{-H_V/5} \quad (1)$$

where D is the effective diameter, $C = 1330 \pm 18$ km is a constant[13], and $H_V = 3.16 \pm 0.12$ mag is Hi'iaka's absolute magnitude, at the time of the

Table 1 | Information about the occulted stars

Occultation date	Designation Gaia EDR3 UCAC4	Coordinates[a] Right Ascension Declination	Magnitudes Gaia catalog UCAC4 [51]	Stellar diameter[b] in *V*-band at Hi'iaka's distance	Hi'iaka's distance (au)
2021-04-06	12294167318702112 00 531-055227	$14^h\ 24^m\ 28^s.6760$ +16° 06' 30".952	$G = 12.628$ $V = 12.824$ $K = 11.000$	~ 0.026 mas ~ 0.935 km	49.394
2021-04-16	12293361883481838 08 531-055209	$14^h\ 23^m\ 52^s.5983$ +16° 10' 40".237	$G = 12.428$ $V = 12.585$ $K = 10.981$	~ 0.025 mas ~ 0.913 km	49.371

[a]Gaia EDR3 coordinates corrected from proper motion for the occultation date.

[b]Estimated from the V and K magnitudes of the star, using equation $\theta = \frac{10^{0.5+0.264(V-K)}}{10^{V/5}}$ [52].

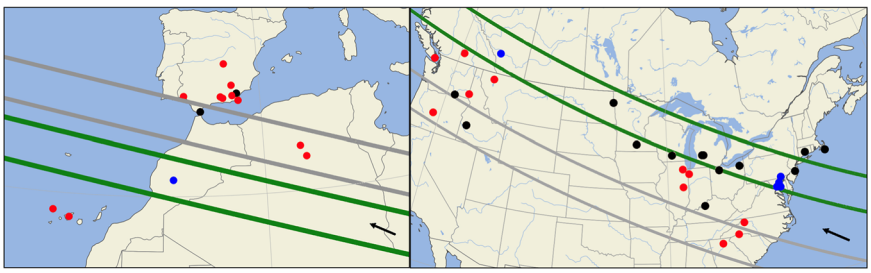

Fig. 1 | Maps showing the locations of the observatories involved in the observing campaigns on April 6th (left) and 16th (right). Blue dots indicate positive detections of the stellar occultation, red dots indicate no detection of the stellar occultation, and black dots indicate no observations due to bad weather or technical problems. Green lines indicate the final shadow path of Hi'iaka considering the respective projected diameter for each event (370 and 360 km for the left and right plots, respectively) while the gray lines show the predicted path. The black arrows located at the bottom right corner of the maps depict the sense of motion of the shadow path. These maps were generated using the SORA package (https://sora.readthedocs.io/latest/).

occultation. The value of H_V was determined as described in the Methods section, accounting for the instantaneous H_V corresponding to the rotational phase. Using this approach, we obtained an albedo value of 0.74 ± 0.15.

Discussion

The high geometric albedo of Hi'iaka (0.74 ± 0.15) is among the larger values within the TNO population[14]. The derivation of this high geometric albedo was made using the equivalent diameter from the occultations and the absolute magnitude of Hi'iaka was determined using 5 different methods (see Methods Section). These are the two parameters that appear in Eq. 2 for the geometric albedo.

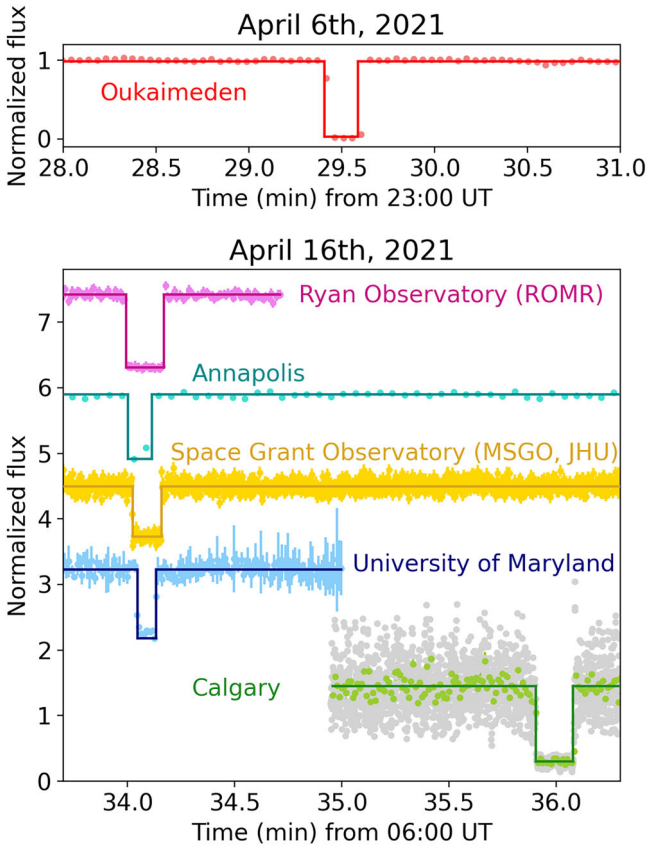

Fig. 2 | Light curves of the positive detections from April 6th (top panel) and April 16th (bottom panel), 2021. Observational data are represented by colored points with their corresponding uncertainties in the same color, with the exception of RAO for which the standard deviation of the data was used as the uncertainty. The error bars for the Annapolis data are smaller than the symbol size and therefore not visible in the figure. The square-well fit models for each light curve describing the occultation of the star are depicted by the solid, colored lines. In the bottom panel, offsets have been applied in the y-axis for clarity. Light curves are plotted in time as seen from each observatory. No residual flux is seen during the occultation.

It is surprising that the geometric albedo of Hi'iaka is higher than that of the object from which it presumably originated (Haumea's albedo is 0.51 ± 0.02[5];). Hi'iaka is currently thought to have formed from the proto-Haumea after a geophysically-driven rotational fission[3,15] or from a collisionally induced rotational fission (e.g.[16],) rather than from a catastrophic collision[17]. Therefore, it is expected that the composition of Hi'iaka should be similar to that of the mantle of Haumea, which is dominated by water ice[18]. Nevertheless, the high geometric albedo of Hi'iaka is consistent with a re-evaluation of the thermal data from the Haumea system using the occultation-determined size and shape[19]. In that re-analysis it was shown that the amplitude of the rotational-thermal light curve requires Haumea's satellites to be highly reflective so that their thermal contributions become very small. In fact, the thermal modeling gives the best results with a Hi'iaka of roughly 300 km in diameter, consistent with our occultation-derived size.

It must also be noted that water ice spectral features in Hi'iaka's spectrum are deeper than those of Haumea itself ([7,20], also from private communication with Jonathan Lunine using data from the JWST 1273 GTO program), where the equivalent depth of the water ice bands is shown to be larger for Hi'iaka than for Haumea (80% versus 60%, respectively). This might mean that the water ice in Hi'iaka could be fresher or purer than that of Haumea or have particle sizes larger than those on Haumea's surface. The very large geometric albedos of the icy Saturnian satellites Enceladus and Tethys come from water ice surfaces with ice particle sizes in the range of 50–100 μ m (see[21,22]). In summary, it might be possible that the water ice particles on Hi'iaka are similar to those of Enceladus and Tethys, yielding a higher albedo compared to Haumea. Whether there is a resurfacing mechanism other than collisions remains to be seen. Cryovolcanism does not seem very likely in a body of around 400 km in diameter, according to simulations of its internal structure that show no significant heating from radionuclides[23] in this size range nor from heat generated through the tidal interaction with Haumea. Differentiation could occur for a rock-to-ice ratio over 0.8, which due to Hi'iaka's theorized formation scenario and the density we obtained (see below) does not seem very likely.

Using the 3D shape obtained through our fit, we obtained a volume-equivalent diameter of 370 ± 20 km. The modeling work of[4] is subject to a degeneracy between Haumea's J2 and Hi'iaka's mass, meaning the modeling results for Hi'iaka's mass cannot necessarily be trusted. We instead use a mass of $16 \pm 2 \times 10^{18}$ kg calculated by[3] assuming Haumea's J2 is 0.16, which is reasonable for a differentiated body. We obtain a density of 640 ± 80 kg m^{-3}. This density is consistent with that expected for a TNO of this size[24] and is also compatible with the idea that Hi'iaka was re-accumulated from the mantle of Haumea after rotational fission or a non-catastrophic collision. The density of

Table 2 | Ingress and egress timings for April 6th and 16th, 2021

Date	Observatory	Ingress (UT)	Egress (UT)	Chord size (s)	σ (mag)
April 6th	TRAPPIST North	23 : 29 : 24.04 ± 0.03	23 : 29 : 34.99 ± 0.02	10.95 ± 0.04	0.014
April 16th	ROMR	06 : 33 : 59.6 ± 0.3	06 : 34 : 10.1 ± 0.3	10.5 ± 0.4	0.05
	Annapolis	06 : 34 : 00.1 ± 0.7	06 : 34 : 06.9 ± 0.7	7 ± 1	0.1
	MSGO (JHU)	06 : 34 : 01.379 ± 0.006	06 : 34 : 09.54 ± 0.04	8.14 ± 0.04	0.088
	UM	06 : 34 : 02.78 ± 0.04	06 : 34 : 08.04 ± 0.04	5.26 ± 0.06	0.089
	RAO	06 : 35 : 54.3 ± 0.2	06 : 36 : 04.8 ± 0.2	10.6 ± 0.3	0.14

In this table, σ corresponds to the data standard deviation calculated from the data prior to and after the occultation.

https://doi.org/10.1038/s41467-025-65749-1

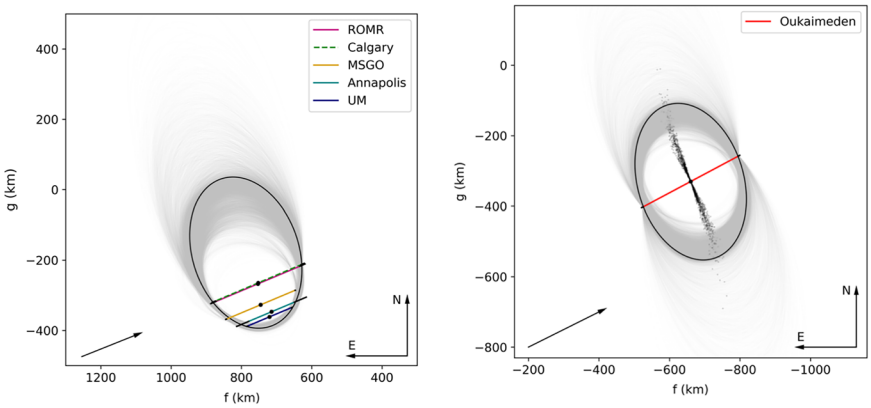

Fig. 3 | Chords and projected ellipses from the ellipsoidal fits to Hi'iaka's shape as observed during the two stellar occultations, shown with respect to the offsets between Hi'iaka's observed positions and its predicted positions from the Miriade ephemeris combined with Haumea's JPL#110 orbit. Left panel: The black ellipse represents the best fit to the positive chords from the stellar occultation on April 16th using least-squares minimization. The gray shaded region represents the solutions from the Monte Carlo simulations. The black arrow at the bottom shows the direction of the body motion. The segments of different colors correspond to the chords from the observing sites indicated in the legend (using the nomenclature of Table 2). Right panel: The single positive chord from the occultation on April 6th is shown (red line) fitted to the ellipses obtained after projecting the 3D model to the corresponding rotational phase at the moment of the April 6th occultation. The small black dots indicate the center of the ellipses. In both panels the errors of the chords are present but may be too small to see.

Table 3 | Details of the positive and closer negative detections on April 6th, 2021

Site (MPC Code) City Country	Latitude (N) Longitude (W) Altitude (m)	Telescope Aperture Detector/instrument Synchronization	Filter T_{exp} (s) T_C (s)	Detection Observers
TRAPPIST North (Z53)	31.2061	60 cm	None	Positive Emmanuel Jehin
Oukaïmeden	7.8664	-	2	
Morocco	2,751	-	2.87	
TAR	28.301	46 cm		Negative Javier Licandro
Tenerife	16.510			
Spain	2,390			
LT (J13)	28.812	2 m		Negative Robotic
La Palma	17.879			
Spain	2,396			
CRAAG (008)	33.32626	279 mm	None	Negative Djounai Baba Aissa
Bellil	3.13157	WATEC 910 HX/RC CCIR PAL		
Algeria	801			
CRAAG (008)	32.48490	279 mm	None	Negative Zaki Grigahcene
Melika	3.68656	WATEC 910 HX/RC CCIR PAL		
Algeria	546			

Abbreviations are defined as follows: International Astronomical Union Minor Planet Center Observatory Code (MPC Code); Liverpool Telescope (LT); Center of Research in Astronomy, Astrophysics and Geophysics - Algiers Observatory (CRAAG); cycle time (i.e., time between exposures (T_{exp}); exposure time (T_C).

the material in Haumea's mantle is estimated to be around 1100 kg m^{-3}. If Hi'iaka was formed from the same icy material flung off due to Haumea's fast rotation, then the re-accumulation of this material into a satellite would result in a very porous, icy object, compatible with the calculated density. It is well known that the composition of moons formed after catastrophic collisions would be mainly that of the impactor, not that of the target, which is one of the deficiencies of the initial formation models of a catastrophic collision (see, e.g.[25],). Additionally, Hi'iaka's rotational light curve amplitude has not changed over the last 15 years, which may indicate an obliquity close to 0°[22], and also supports the stages 3 and 4 of the formation scenario described in[16].

Regarding the three-dimensional shape obtained for Hi'iaka, it must be noted that it is not consistent with that of a homogeneous body in hydrostatic equilibrium for the resulting density and the known rotation period. A body with a density of ~ 600 kg m^{-3} rotating in ~ 9.68 h should have adopted a Maclaurin shape according to the figure of equilibrium formalism in[26]. Stellar occultation results have found this to be a common outcome for most TNOs for which 3D shapes have been obtained, see for instance the case of Haumea[5] or 2003 VS_2[27]. In the case of Hi'iaka and 2003 VS_2, contrary to Haumea, we do not expect differentiation due to their relatively small sizes. Differentiation for ice bodies with radii larger than 200 km was studied by[23], and found to be non-negligible. However, it is small enough that the deviation induced by differentiation in these bodies would not be detectable. The most likely reason behind this deviation of hydrostatic equilibrium shape is probably some material strength. Therefore, Hi'iaka, similar to many other bodies, may have an equilibrium shape that deviates from hydrostatic equilibrium, resulting in lower density values as obtained in this work.

Methods

Prediction of the stellar occultations

The two stellar occultations by Hi'iaka in April 2021 were predicted using the Gaia EDR3 catalog[28] and the orbital elements given by the Jet Propulsion Laboratory (https://ssd.jpl.nasa.gov/horizons/app.html#/).

The first occultation, on April 6th, 2021, was predicted to cross North Africa from Somalia to Morocco; the second occultation on April 16th, 2021, was predicted to cross the continental United States from North Carolina to Oregon. These predictions had relatively large error bars, with the main source of error coming from the position of Haumea. In order to refine the prediction of the shadow paths, we took additional images of the unresolved Haumea-Hi'iaka system using different ground-based facilities, as described below.

On February 26th, 2021, we obtained images with the 2-m Liverpool Telescope (LT) at La Palma with the IO:O instrument, the Sloan *r* filter, and 300-second integration times. On March 10th, 14th, 15th, 17th, 22nd and 23rd, and April 10th, 2021, observations were obtained with the Sierra Nevada 1.5-m telescope using the 2k × 2k CCD camera in 2 × 2 binning mode with 300-second integration times and the Johnson *R* filter. On April 10th, 2021, we obtained observations from the 1.6-m Pico dos Dias telescope using the Andor Ixon 4269 CCD with the Johnson *R*

https://doi.org/10.1038/s41467-025-65749-1

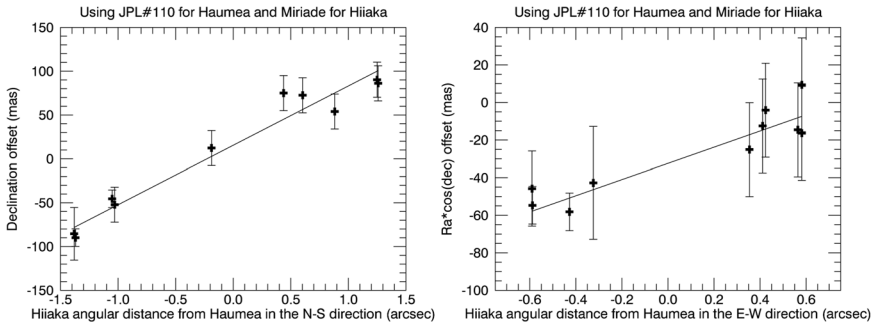

Fig. 4 | Residuals of the astrometric data to Haumea's orbit versus the angular separation of Hi'iaka with, respect to Haumea obtained from the Miriade service. Each point corresponds to the median of the residuals, obtained per night per telescope. The line depicts a linear fit to the data points.

filter and 300-second integration times; and on April 17th observations were obtained with the DLR 4kx4k CCD camera of the Calar Alto observatory 1.2 m telescope, using exposure times of 300 s, binning 2×2 and the Johnson R filter.

We obtained high-accuracy astrometric data to anchor Haumea's JPL#110 orbit as explained in[29]. From each observing night and telescope, we obtained the position of the barycenter of Haumea with respect to Hi'iaka, resulting in a total of 10 points. The photocenter of Haumea plus Hi'iaka rotates around the barycenter, so when plotting the photocenter residuals with respect to Haumea's orbit versus the position of the satellite (which was obtained from the Miriade service), we were able to determine the position of the barycenter in right ascension and declination using linear fits (which is the same method used to predict the stellar occultation by Haumea in 2017[5], see Fig. 4). A similar derivation of the offsets can be found in[30], where the available orbit at that time was JPL#108 (instead of the more recent JPL#110 as in this work). We note that Namaka is not detectable at the level of precision achievable with the data. On one hand, Namaka's mass is one order of magnitude smaller than Hi'iaka's, which translates to perturbations in the period of a few minutes of time. On the other hand, the difference in brightness between Haumea and Namaka (which according to[4] is around 100 times lower) translates into an effect of around 7 mas. This level of precision is possible thanks to the high astrometric accuracy of the Gaia EDR3 catalog, which allows TNO positional measurements from the ground with a typical accuracy of 10 mas, provided that the SNR is high enough and that we corrected for differential chromatic refraction by using a similar approach as in[31] using magnitudes and color information from the Gaia DR3 catalog for the stars in the field of view. The offsets with respect to JPL#110 are 15 ± 6 milliarcseconds (mas) and -32 ± 6 mas in declination and right ascension, respectively. The resulting prediction for the April 6th occultation after this analysis moved northward with respect to the initial prediction, now crossing from Somalia to the north of Morocco and including the southern portion of the Iberian Peninsula, with an uncertainty of 8 mas.

Although the star to be occulted by Hi'iaka was adequately bright ($V = 12.8$ mag), the region of the predicted shadow path was not home to a large number of telescopes. Most of our telescopes were located in Spain (mainland and Canary Islands). We obtained one positive detection from Morocco and several negatives from Algeria and Spain. The predicted and actual, reconstructed shadow paths can be seen in the left panel in Fig. 2, with the center path being determined as in[32].

A new analysis for the second occultation, considering the motion of Hi'iaka about the system barycenter and the stellar occultation on April 6th, moved the predicted shadow path northward with respect to the initial prediction, resulting in a path that crossed North America from New York (United States of America) to British Columbia (Canada) with an error bar of 8 mas. Since the star for the second stellar occultation by Hi'iaka was also very bright ($V = 12.6$ mag), the event was favorable even for very small telescopes. We arranged a campaign with professional and amateur observers all over the United States and Canada to record the stellar occultation. The final, real path deviated from the last predicted path by 24 mas (see Fig. 2, right panel). The occultation of this star was positively observed from six different telescopes, but only five produced useful data.

Stellar Occultation Observations and Data Reduction

Here we describe the most relevant observations for the analysis of the stellar occultation, i.e., the observations where the detection was positive. Note that in both events, no negative detections were used to constrain the body because they were not close enough to constrain Hi'iaka's size and shape.

In both occultations, we obtained time-series imaging or video recording using each of the telescopes and cameras listed in Tables 3 and 4. All computers were synchronized using Network Time Protocol (NTP) servers or Video Time Inserters (VTI), which were time-synchronized by Global Positioning System (GPS) devices. The acquisition time of each image was inserted on the corresponding image header, while for the video acquisition the time was written over the frames. All charge-coupled device (CCD) imaging time series covered at least 15 minutes before and after the predicted occultation time in order to obtain both a good baseline to characterize the occultation and the noise level before and after the event.

If possible, no filters or very wide bandpass filters were used to maximize the signal-to-noise ratio (SNR) of the star to be occulted. In the case of the FITS images, they were calibrated using standard procedures for dark/bias subtraction and flat-fielding correction. No standard calibration was applied to the data sets obtained in video format.

For the FITS images, we performed synthetic aperture photometric techniques using DAOPHOT routines[33] and searched for the optimum aperture to minimize the scatter of the photometry. The photometry was performed on the occulted star (blended with Haumea's system) with respect to reference stars in the images in order to monitor and compensate for small transparency fluctuations or seeing variations, with the exception of Morocco's light curve, for which only the occulted star appears in the FoV. In the latter case, we normalized the light curve (flux versus time) using the LightCurve module within the SORA package[34]. For all other cases, the light curves were normalized by dividing the relative flux by the mean relative flux level of the blended star plus Haumea's system (outside of the occultation event). Photometric errors were obtained with the DAOPHOT routines that use Poisson noise estimations. If the gain values (number of electrons per count) of the camera devices were not known, the individual photometric errors were rescaled using the standard deviation

https://doi.org/10.1038/s41467-025-65749-1

Table 4 | Details of the positive and closer negative detections on April 16th, 2021

Site City, State Country	Latitude (N) Longitud Altitude (m)	Telescope Aperture Detector/instrument Synchronization	Filter T_{exp} (s) T_C (s)	Detection Observers[a]
ROMR	39.8449758	356 mm	None	Positive RK, AR & BE
Holtwood, Pensilvania	-76.2839233	QHY174M	0.5	
USA	185.8	GPS	1	
Conti Private Observatory	38.936961	280 mm	*V*	Positive Dennis Conti
Annapolis, Maryland	-76.490728	StarlightXpress H694	2	
USA	4	NTP server	3.44	
MSGO (JHU)	39.331780	508 mm	BYL	Positive AV & ZR
Baltimore, Maryland	-76.623250	ASI6200MM	0.075	
USA	93.3		0.150	
UMD	39.0021	152 mm	None	Positive EW & BH
College Park, Maryland	-76.9560	GX-FW-28S5M-C	0.533	
USA	53	GPS	0.533	
RAO[b] (661)	50.868039	406.4 mm	None	Positive PL, RM & LM
Calgary, Alberta	-114.291142	Sony Alfa 7 s	2	
Canada	1,272		2	
RECON	41.270533	1.83 m	None	Negative AWR
Kelowna, British Columbia	-87.375261		3.5	
Canada	205			
Plaskett Telescope	48.520286	1.83 m		Negative Dmitry Monin
Victoria, British Columbia	-123.418147			
Canada	230			

Abbreviations are defined as follows: Ryan Observatory at Muddy Run (ROMR); Maryland Space Grant Observatory (MSGO); John Hopkins University (JHU); University of Maryland Astronomy Observatory (UMD); Rothney Astrophysical Observatory (RAO); Baader Yellow Longpass (BYL); exposure time (T_{exp}) cycle time (i.e., time between exposures T_C).

[a]Observer name's abbreviations are defined as follows: Alex de la Vega (AV), Zafar Rustamkulov (ZR), Elizabeth Warner (EW), Bryan Holler (BH), Denis Conti (DC), Roxanne Kamin (RK), Al Ryan (AR), Bernie Earls (BE), Phil Langill (PL), Ruben Morales (RM), Larry McNish (LM), Adam W. Rengstorf (AWR).

[b]Data from RAO were binned to reduce noise, with individual exposure times of 0.625 s.

of the data separating the resulting light curves in two regions, outside and inside the event.

In the case of RAO (Rothney Astrophysical Observatory, Calgary) a MPEG Transport Stream video file was provided. We converted this file to the AVI file format using ffmpeg software in order to reduce and analyze it with PyMovie/PyOTE[35]. An acoustic time signal from a time signals simulator (also known as WWV) was recorded along with the video on the audio track. Specific time markers (based on the acoustic time signal) were set before and after the occultation (by ear) inside PyOTE in order to get the absolute time of the recording and of each individual frame. In this case, the photometric errors were obtained from the standard deviation of the data by evaluating the parts prior to and after the occultation, and the occultation itself, independently.

Analysis of the positive detections of the stellar occultations

From the positive-detection light curves, we obtained the time at which the star disappeared and reappeared (also known as ingress and egress timings, respectively) by fitting the light curves to a square-well function in which the main parameters of the model were the drop in brightness and the times of the ingress and egress. The uncertainties were calculated by considering the errors in the photometric measurements and the cycle time, which were the two largest sources of uncertainty. The Fresnel diffraction (see[36]) was evaluated using the Fresnel scale equation:

$$F = \sqrt{\frac{\lambda \Delta}{2}}, \tag{2}$$

where $\lambda = 600$ nm was the average central wavelength for the CCD observations, and Δ was Hi'iaka's geocentric distance (49.4 au), which resulted in $F = 1.5$ km. On the other hand, the stars' angular diameters were both around 0.9 km (see Table 1). Both scales are smaller than the scale of sampling at Hi'iaka's distance from our measurements, given that the shortest cycle time achieved in one of the observatories was 0.15 s, which corresponds to 3.8 km at the 25.67 km/s average speed of Hi'iaka in the sky plane. The remaining observatories had even poorer sampling.

In the cases in which the ingress and/or egress occurred during a dead-time, the timings were calculated by obtaining the time from the previous image (when the camera was reading the data) and adding the cycle time $T_C/2$ (taking into account that the used photometric pipelines provide the time at the middle of the exposure) which is required to locate the timing at the middle of the dead-time. The uncertainty in this case is calculated as half of the dead-time interval.

Rotational Light Curve Observations and Data reduction

Observations and data reduction for Hi'iaka's rotational light curve. A total of four runs were carried out to obtain time-series photometric data of the Haumea-Hi'iaka system during 2021 and 2022 using two different ground-based observatories:

- The 1-m telescope Artemis located at Teide observatory in Tenerife (Canary Islands, Spain) during May 2021 and March and May 2022, whichis part of the SPECULOOS robotic telescope network[37]. The camera located at this telescope is an Andor iKon-L of 2048 × 2048 pixels providing a field of view (FoV) of 12′×12′, and a pixel scale of 0.35″ pixel^{-1}. Images were acquired with the Exo blue cutting filter and an exposure time of 240 s in order to obtain the highest possible SNR (with an average of ∼ 400 for each night). We used the 2 × 2 binning mode during the first night in May 2021, however, we realized that no binning provided a higher SNR; therefore, we switched to 1×1 binning from that night forward. Each night (with the exception of March 29, 2022) we acquired more than one complete rotation period of Haumea, which is ∼ 3.9 h.
- The 1.23-m telescope at Calar Alto Observatory in Almería (Spain). A 4 × 4 DLR-MKIII CCD camera is located at this telescope with a FoV of 21.5′×21.5′ and a pixel scale of 0.32″ pixel^{-1}. Images were acquired with the Johnson *R* filter with an exposure time of 300 s, and we obtained an average SNR of ∼ 400. Images were taken with 2×2 binning.

For both telescopes, the image calibration was performed following standard procedures of bias and/or dark subtraction and flat field correction. Stars with high SNR were selected and checked for variability. Given the slow speed of Haumea on the sky (1′ d^{-1}) we could use the same set of comparison stars within the same run, with the exception of March 2021, for which the first night (when 2 × 2 binning was used) was treated separately.

For the Artemis telescope, we performed synthetic aperture photometry to measure the flux of the target and stars with IRAF software and then calculated differential photometry with Python scripts. Finally, we obtained the Johnson-Cousins *R* magnitudes by performing absolute calibration using the PHOTOMETRYPIPELINE[38] with the SDSS-R9 catalog. In the case of the 1.23-m telescope at Calar Alto, we used our own codes written in IDL to perform relative

photometry on the images (as done in, e.g.[39,40],). No absolute calibration was done in this case.

To our knowledge, this is the first time that the rotation light curve of a known satellite was obtained from photometric data of a TNO system by removing the shape model of the main body.

Rotational Light-Curve Results

To fully constrain Hi'iaka's physical properties, knowledge of the rotational phase for both stellar occultations was required. Hi'iaka's rotational properties were first studied in[6] using data from the Hubble Space Telescope (HST) in 2009 and the Magellan Baade telescope at Las Campanas Observatory in Chile in 2010. They obtained a double-peaked rotational light curve with a period of approximately 9.8 h, with the single significant digit after the decimal point indicating an uncertainty on the order of 0.1 h (no formal errors were provided). At this level of uncertainty, rotational phase information becomes unreliable after only a few days; considering the one-decade time-gap between these rotational light curves and the stellar occultations, all rotational phase information was completely lost. Therefore, we needed to carry out new photometric observations close in time to the stellar occultations in order to accurately determine Hi'iaka's rotational phase at the time of the occultations to be able to reconstruct Hi'iaka's 3D shape. A detailed description of these observations and the processing performed on these images can be seen in the supplementary material in the Methods Section.

The ground-based telescopes and instruments used to obtain Hi'iaka's rotational light curve did not have the spatial resolution to separate Haumea and Hi'iaka. Therefore, we needed to extract Hi'iaka's rotational light curve from Haumea's. We folded all data using the well-known rotation period of Haumea, 3.915341 ± 0.000005 h[41], and then fit the data to a fourth-order Fourier function. While a second-order function would reproduce the overall shape of the Haumea rotational light curve, a fourth-order function also accounts for the most prominent surface heterogeneities detectable within the uncertainty of our data (a similar procedure was done in[39]). The residuals from the fit to the observational data contain Hi'iaka's rotational light curve, which can be seen by folding the residuals using Hi'iaka's rotation period from[6].

We applied the Lomb periodogram technique[42–44] to the residuals of our observational data as implemented in the Scipy package of Python (see Fig. 3, left panel). For a single-peaked rotational light curve, the maximum spectral power corresponds to a rotation period of 4.84 h. However, we are aware of the triaxial shape of Hi'iaka from[6], which means that the rotational light curve should present two peaks due to shape effects. Therefore, the rotation period is double the value obtained from the periodogram, which results in 9.68 ± 0.02 h. The uncertainty of the rotation period was estimated by fitting a Gaussian function to the peak in the Lomb periodogram that provides the most probable rotation period and calculating the full width at half maximum. The final rotational light curve of Hi'iaka can be seen in Fig. 3, right panel.

Three-Dimensional Model

The occultation times with their 1-σ uncertainties were translated to a bi-dimensional frame (f,g) with the origin on the object's position as given by its ephemeris at the instant of closest approach. In this work, we used the Hi'iaka ephemeris from the Miriade service combined with the Haumea ephemeris from JPL (orbit ID #110). Each immersion and emersion pair, translated to the (f,g) plane, provided one precise measurement across the object's profile, given in kilometers (km), which hereafter is called a "positive chord". When a large enough number of positive chords, plus close non-detections (hereafter "negative chords") are available, it is possible to accurately reproduce the object's instantaneous profile as observed during the occultation at a sub-kilometer level of accuracy[32,44]. However, the negative chords obtained in the events described in this work were not close enough to the body to provide constraints on the object's profile. Additionally, objects larger than 200 km are expected to adopt a shape under hydrostatic equilibrium[45], either a McLaurin or Jacobi ellipsoid shape[26]. The projection of such shapes into the sky plane will directly translate into an ellipse, thus being reasonable to fit an ellipse to the extremities of the positive chords obtained on April 16th. We cannot fit an ellipse to the occultation on April 6th because, to avoid degeneracy, at least five points are required and only two were available.

Considering that Hi'iaka orbits Haumea in the same equatorial plane as Haumea's ring, we can reasonably assume that the satellite's aspect angle (the angle between the line of sight and the body's spin axis) would fall within the same range as Haumea's. Based on our current knowledge about the satellites of large TNOs, a putative inclination of Hi'iaka's spin axis relative to Haumea is unlikely. Therefore, the methodology used in this work consists of creating a large set of 3D models with a homogeneous surface brightness and random values for the a, b, and c true semi-axes using the equations provided by[46]. We also made use of the known rotational light curve from[6], new observations to obtain the rotational phase at which the stellar occultations occurred, and Haumea's aspect angle to constrain Hi'iaka modelled tridimensional shape.

The simulated models had an aspect angle ranging from 60° to 80° and, assuming a homogeneous albedo distribution, a rotational light curve amplitude between 0.17 and 0.25 mag. The range of aspect angles and light curve amplitudes were chosen to account for the many uncertainties regarding Hi'iaka's orientation, here assumed to be similar to Haumea's. Note that the rotational light-curve amplitude was taken from[6] because rotational light curves obtained closer to the event were not directly obtained from the satellite but rather as an indirect measurement through the observation of the system. However, we do not expect appreciable changes in Hi'iaka's rotational light curve amplitude, since its rotational light curve did not change appreciably between 2007 and 2020[47]. The amplitude was calculated with Eq. 1 in[25], with a tolerance of 0.03 mag applied to accept the ellipsoids, considering the uncertainty in the exact scattering law and potential deviations from a perfect ellipsoid. Finally, the 3D models were rotated to match the phase obtained in the previous section for the April 16th occultation and compared to the occultation chords. We used a Monte Carlo approach with 10000 simulated models, a gaussian distribution of the occultation error bars, and a minimization procedure that searched for the minimum quadratic separation between the chord extremity and the fitted model.

The resulting 10000 ellipsoids that, projected to the sky plane at the given rotational phase, better reproduced the profile observed on April 16th, were also rotated to Hi'iaka's rotational phase at the time of the April 6th occultation. The projected ellipse parameters can be seen in Table 5. The ellipses were then compared to the single-chord detection by using least-squares and leaving only as free parameters the center (f,g). Due to the length and accuracy of this single-profile measurement, most of the center solutions (~90%) fall very close to the positive chord, implying a potential equatorial detection (Fig. 4), within the error bars.

The distribution of the parameters for the 10000 tridimensional simulated models is presented in Supplementary Fig. 1. The ellipse parameter distributions for April 16th and April 6th are shown in Supplementary Fig. 2 and 3, respectively. Note that due to the distribution of (f,g), and the plot scale needed for Supplementary Fig. 2, the histogram peak is difficult to see behind the red vertical line. Additionally, the non-gaussian distribution for the histogram of x and y parameters in Supplementary Fig. 2 can be explained by the additional constraints needed to obtain the object's profile from a single-chord detection.

Table 5 | Elliptical parameters of the projected body shape from the best-fit in terms of least-squares minimization

Event	a_I (km)	b_I (km)	θ (deg)	f (km)	g (km)	D_I (km)	D (km)	p_V (%)
16th	220 ± 40	150 ± 10	112 ± 3	790 ± 10	−180 ± 40	360 ± 30	360 ± 20	80 ± 10
6th	230 ± 40	150 ± 10	110 ± 10	−660 ± 10	−330 ± 40	360 ± 30		

Abbreviations are as follows: semi-major and -minor axes of the projected ellipse (a_I, and b_I), position angle of the semi-minor axis of the ellipse (θ), the offsets in the East-West and North-South directions between the predicted and the reconstructed positions of Hi'iaka's center (f and g, respectively), the instantaneous and rotationally-averaged volume-equivalent diameter (D_I, and D), and the geometric albedo (p_V).

Hi'iaka's absolute magnitude H_V

Hi'iaka's absolute magnitude was not straightforward to obtain because our ground-based observations could not resolve the system. It is worth noting that most published values of Haumea's absolute magnitude include not only Haumea but the whole system (Haumea + ring + satellites). Also, when measuring the flux in HST images, the flux of Haumea also includes the ring because HST is not able to resolve this part of the system. In order to calculate Hi'iaka's absolute magnitude we first obtained Hi'iaka's relative magnitude with respect to Haumea + rings in five different ways (in the following points Haumea refers to "Haumea + rings"):

- Ref. 48 obtained resolved images of Haumea and Hi'iaka from which they obtained a magnitude difference of 2.76 ± 0.18 in the J band. This value accounts for the rotational variability of Haumea, since they averaged several mea-surements taken along half of the rotational period of Haumea. Other authors have obtained the relative brightness of the Haumea - Hi'iaka system from resolved images[1,48], however, they did not account for Haumea's rotational variability, which introduces large errors in the relative brightness between the objects. Therefore, we considered as the best estimated relative magnitude the one from[49]. Assuming Hi'iaka's spectrum is very similar to Haumea (a reasonable assumption since their colors are also very similar[8]), the relative magnitude between Haumea and Hi'iaka in H band should be the same as in V band.
- From resolved HST images at visible wavelengths[4], report a factor of ∼ 10 difference in flux of Haumea compared to Hi'iaka, which translates to 2.5 mag.
- Haumea's rotational light curve amplitude, Δm, measured from resolved HST images of the system is 0.320 ± 0.006 mag[50]. On the other hand, Haumea's Δm measured from the ground (i.e., including the brightness of Hi'iaka) in the same year of the HST images was 0.29 ± 0.01 mag (using the models in[5]). The difference in amplitude is moderated by the presence of Hi'iaka, which is always contributing to the flux of the unresolved system. Using the equation $\Delta m = -\frac{5}{2}\log\frac{F_{\min}}{F_{\max}}$, where $F_{\min}$ and $F_{\max}$ are the flux at minimum and maximum brightness of the rotational light curve, respectively, we calculated the variation in flux needed to obtain an amplitude of 0.32 mag of ∼ 34%. In order to decrease that amplitude to 0.28, we needed to introduce an extra flux of ∼ 15%. For Hi'iaka to contribute 15% of Haumea's flux, the relative magnitude between both objects must be 2.1. If we apply the same exercise considering the uncertainties in each case, then the relative magnitude of Hi'iaka with respect to Haumea should be between 1.54 and 2.55 mag.
- Similar to the strategy in the previous point, but this time using Hi'iaka's rotational light curve, we know that Hi'iaka's rotational light curve amplitude from HST images is 20% (Δm = 0.218 ± 0.002 mag), while the amplitude from our ground-based observations obtained as an indirect measurement by removing Haumea's contribution to the data is 0.012 mag. This means that Hi'iaka's rotational light-curve is being "smoothed" by the flux reflected by Haumea and the remaining components of the system, resulting in a noticeably "flatter" rotational light-curve. In order to obtain such a decrease in the amplitude of the rotational light curve of Hi'iaka, we need an object 17 times brighter than Hi'iaka. This means a difference of 3.1 mag. We note that the amplitude of the rotational light curve in 2021 (if taken with HST, i.e., when the ground-based observations were taken) may be smaller than 20%, and therefore this last value of relative magnitude between Haumea and Hi'iaka may be overestimated.
- The photocenter of the system should be defined by the following equation:

$$Photocenter = \frac{I_H x_H + I_h x_h}{I_H + I_h} \tag{3}$$

where I_H and I_h are the intensities of Haumea and Hi'iaka, respectively, and x_H and x_h are the positions of Haumea and Hi'iaka, respectively. If $f = I_h/Ix_H$, then:

$$Photocenter = \frac{I_H(x_H + f x_h)}{I_H(1+f)} = \frac{x_H + f x_h}{1+f} \tag{4}$$

If we set the coordinate system at the position of Haumea, then $x_H = 0$, so

$$Photocenter = \frac{f x_h}{1+f} \tag{5}$$

At the maximum distance of Hi'iaka from Haumea $x_h = 1.4''$, whereas the photo-center position is $0.09''$ (as can be seen in Fig. 1). Thus, $f = 0.09/(1.4 - 0.069)$. This corresponds to a 2.916 mag difference between Hi'iaka and Haumea. We note that the photocenter revolves around the barycenter, and that the distance from Haumea to the barycenter is $\sim 0.005''$, therefore, if the photocenter reaches $0.09''$ from the barycenter, Haumea would be an extra $0.01''$ closer to Hi'iaka (this is assuming that the mass ratio between Haumea and Hi'iaka is 100). In this case, $f = 0.06$, which corresponds to 2.899 mag. Therefore, the relative magnitude should be between 2.916 and 2.899 mag.

If we consider the results from all of these methods, we obtain a weighted-average relative magnitude of 2.76 ± 0.12 mag. Using the models in[5] for the absolute magnitude of Haumea + rings, the absolute magnitude in 2021 was 0.45 mag. This means that Hi'iaka's absolute magnitude is 3.21 ± 0.12 mag. The uncertainty has been calculated as the standard deviation of the results from the different methods. This value needs to be corrected by the rotational light curve at the phase of the stellar occultation by −0.05 mag.

Data availability

Source data is available as a Source Data file. This work has made use of data from the European Space Agency (ESA) mission Gaia (https://www.cosmos.esa.int/gaia), processed by the Gaia Data Processing and Analysis Consortium (DPAC, https://www.cosmos.esa.int/web/gaia/dpac/consortium). This research is based on observations collected at the Centro Astronómico Hispano-Alemán (CAHA) at Calar Alto

(Spain), the Liverpool Telescope at the Observatorio del Roque de los Muchachos in the Canary Islands (Spain), the TRAPPIST telescope (Morocco), and the Tx40 telescope at the Observatorio Astrofísico de Javalambre in Teruel (Spain). Source data are provided with this paper.

References

1. Brown, M. E. et al. Keck observatory laser guide star adaptive optics discovery and characterization of a satellite to the large kuiper belt object 2003 EL61. *Astrophys. J.* **632**, L45–L48 (2005).
2. Leinhardt, Z. M., Marcus, R. A., Stewart, S. T. The formation of the collisional family around the dwarf planet Haumea. *Astrophys. J.* **714**, 1789–1799 (2010).
3. Proudfoot, B. & Ragozzine, D. The formation of Haumea and its family via binary merging. *Nat. Commun.* **13**, 2262 (2022).
4. Ragozzine, D. & Brown, M. E. Orbits and Masses of the Satellites of the Dwarf Planet Haumea (2003 EL61). *Astron. J.* **137**, 4766–4776 (2009).
5. Ortiz, J. L. et al. The size, shape, density and ring of the dwarf planet Haumea from a stellar occultation. *Nature* **550**, 219–223 (2017).
6. Hastings, D. M. et al. The Short Rotation Period of Hi'iaka, Haumea's Largest Satellite. *Astron. J.* **152**, 195 (2016).
7. Barkume, K. M., Brown, M. E. & Schaller, E. L. Water Ice on the Satellite of Kuiper Belt Object 2003 EL61. *Astrophys. J.* **640**, L87–L89 (2006).
8. Fraser, W. C. & Brown, M. E. NICMOS photometry of the unusual dwarf planet Haumea and its satellites. *Astrophys. J.* **695**, L1–L3 (2009).
9. Vara-Lubiano, M. et al. The first multichord stellar occultation by the trans-Neptunian Binary (82075) 2000 YW134. In Europlanet Science Congress, EPSC2022-1048 (2022).
10. Jehin, E. et al. TRAPPIST: TRAnsiting Planets and PlanetesImals Small Telescope. *Messenger* **145**, 2–6 (2011).
11. Magnusson, P. Distribution of spin axes and senses of rotation for 20 large asteroids. *Icarus* **68**, 1–39 (1986).
12. Proudfoot, B. C. N. et al. Beyond Point Masses. III. Detecting Haumea's Non-spherical Gravitational Field. *Planet. Sci. J.* **5**, 69 (2024).
13. Masiero, J. R., Wright, E. L. & Mainzer, A. K. Uncertainties on Asteroid Albedos Determined by Thermal Modeling. *Planet. Sci. J.* **2**, 32 (2021).
14. Müller, T. et al. Trans-Neptunian objects and Centaurs at thermal wavelengths. In Dina Prialnik, Maria Antoinetta Barucci, and Leslie Young, editors, The Trans-Neptunian Solar System, 153–181. (Elsevier, 2020).
15. Ortiz, J. L. et al. Rotational fission of trans-Neptunian objects: the case of Haumea. *Mon. Not. R. Astron. Soc.* **419**, 2315–2324 (2012).
16. Noviello, J. L., Desch, S. J., Neveu, M., Proudfoot, B. C. N. & Sonnett, S. Let It Go: Geophysically Driven Ejection of the Haumea Family Members. *Planet. Sci. J.* **3**, 225 (2022).
17. Campo Bagatin, A., Benavidez, P. G., Ortiz, J. L. & Gil-Hutton, R. On the genesis of the Haumea system. *Mon. Not. R. Astron. Soc.* **461**, 2060–2067 (2016).
18. Pinilla-Alonso, N. et al. The surface of (136108) Haumea (2003 EL_{61}), the largest carbon-depleted object in the trans-Neptunian belt. *Astron. Astrophys.* **496**, 547–556 (2009).
19. Müller, T. et al. Haumea's thermal emission revisited in the light of the occultation results. *Icarus* **334**, 39–51 (2019).
20. Dumas, C., Carry, B., Hestroffer, D. & Merlin, F. High-contrast observations of (136108) Haumea. *A crystalline water-ice Mult. Syst. Astron. Astrophys.* **528**, A105 (2011).
21. Buratti, B. J. et al. Spectral Analyses of Saturn's Moons Using the Cassini Visual Infrared Mapping Spectrometer. In Janice L. Bishop, III Bell, James F., and Jeffrey E. Moersch, editors, Remote Compositional Analysis: Techniques for Understanding Spectroscopy, Mineralogy, and Geochemistry of Planetary Surfaces, 428–441. (Cambridge University Press, 2019).
22. Verbiscer, A. et al. Enceladus: Cosmic Graffiti Artist Caught in the Act. *Science* **315**, 815 (2007).
23. Loveless, S. et al. On the Structure and Long-term Evolution of Ice-rich Bodies. *Astrophys. J.* **927**, 178 (2022).
24. Csaba, K. et al. The mass and density of the dwarf planet (225088) 2007 OR10. *Icarus* **334**, 3–10 (2019).
25. Schlichting, H. E. & Sari, R. The Creation of Haumea's Collisional Family. *Astrophys. J.* **700**, 1242–1246 (2009).
26. Chandrasekhar, S. Ellipsoidal figures of equilibrium. The Silliman Foundation Lectures. (Yale University Press, 1969).
27. Vara-Lubiano, M. et al. The multichord stellar occultation on 2019 October 22 by the trans-Neptunian object (84922) 2003 VS_2. *Astron. Astrophys.* **663**, 17 (2022).
28. Gaia Collaboration et al. Gaia Early Data Release 3. Summary of the contents and survey properties. *Astron. Astrophys.* **649**, A1 (2021).
29. Ortiz, J. L., Sicardy, B., Camargo, J. I. B., Santos-Sanz, P. & Braga-Ribas, F. Stellar occultation by TNOs: from predictions to observations. In Dina Prialnik, Maria Antoinetta Barucci, and Leslie Young, editors, The Trans-Neptunian Solar System, 413–437. (Elsevier, 2020).
30. Peng, Q. Y. et al. CCD astrometric measurements for the dwarf planet Haumea by ground-based telescopes. *Astron. Astrophys.* **672**, A61 (2023).
31. Gomes, D. C. H. et al. Can the Gravitational Effect of Planet X be Detected in Current era Tracking of the Known Major and Minor Planets? *Planet. Sci. J.* **4**, 21 (2023).
32. Rommel, F. L. et al. Stellar occultations enable milliarcsecond astrometry for Trans-Neptunian objects and Centaurs. *Astron. Astrophys.* **644**, A40 (2020).
33. Stetson, P. B. DAOPHOT: a computer program for crowded-field stellar photometry. *Pub. Astron. Soc. Pacific* **99**, 191 (1987).
34. Gomes-Júnior, A. R. et al. SORA: Stellar Occultation Reduction and Analysis. *Mon. Not. R. Astron. Soc.* **511**, 1167–1181 (2022).
35. Anderson, B. PyMovie - A Stellar-Occultation Aperture-Photometry Program. *J. Occ. Astron.* **9**, 9–13 (2019).
36. Roques, F., Moncuquet, M. & Sicardy, B. Stellar occultations by small bodies - Diffraction effects. *Astron. J.* **93**, 1549–1558 (1987).
37. Delrez, L. et al. SPECULOOS: a network of robotic telescopes to hunt for terrestrial planets around the nearest ultracool dwarfs. In Heather K. Marshall and Jason Spyromilio, editors, Ground-based and Airborne Telescopes VII, volume 10700 of Society of Photo-Optical Instrumentation Engineers (SPIE) Conference Series, 107001I (2018).
38. Mommert, M. Photometrypipeline: An automated pipeline for calibrated photometry. *Astron. Comput.* **18**, 47–53 (2017).
39. Fernández-Valenzula, E. et al. The Changing Rotational Light-curve Amplitude of Varuna and Evidence for a Close-in Satellite. *Astropys. J.* **883**, L21 (2019).
40. Fernández-Valenzuela, E., Ortiz, J. L., Duffard, R., Santos-Sanz, P. & Morales, N. 2008 OG19: a highly elongated Trans-Neptunian object. *Mon. Not. R. Astron. Soc.* **456**, 2354–2360 (2016).
41. Lellouch, E. et al. "TNOs are cool": A survey of the trans-Neptunian region. II. The thermal lightcurve of (136108) Haumea. *Astro. Astrophys.* **518**, L147 (2010).
42. Lomb, N. R. Least-squares frequency analysis of unequally spaced data. *Astrophys. Space Sci.* **39**, 447–462 (1976).
43. Zechmeister, M. & Kürster, M. The generalised Lomb-Scargle periodogram. A new formalism for the floating-mean and Keplerian periodograms. *Astron. Astrophys.* **496**, 577–584 (2009).
44. Virtanen, P. et al. SciPy 1.0: fundamental algorithms for scientific computing in python. *Nat. Methods* **17**, 261–272 (2020).

45. Rommel, F. L. et al. A large topographic feature on the surface of the trans-Neptunian object (307261) 2002 MS4 measured from stellar occultations. *Astron. Astrophys.* **678**, 25 (2023).
46. Farinella, P., Paolicchi, P., Tedesco, E. F. & Zappala, V. Triaxial equilibrium ellipsoids among the asteroids? *Icarus* **46**, 114–123 (1981).
47. Fernández-Valenzuela, E. et al. Hi'iaka's physical and dynamical properties using long-term photometric data. In Europlanet Science Congress, EPSC2022–406 (2022).
48. Gourgeot, F. et al. Near-infrared spatially resolved spectroscopy of (136108) Haumea's multiple system. *Astron. Astrophys.* **593**, A19 (2016).
49. Lacerda, P. Time-resolved near-infrared photometry of extreme Kuiper belt object Haumea. *Astron. J.* **137**, 3404–3413 (2009).
50. Lockwood, A. C., Brown, M. E. & Stansberry, J. The Size and Shape of the Oblong Dwarf Planet Haumea. *Earth Moon Planets* **111**, 127–137 (2014).
51. Zacharias, N. et al. VizieR Online Data Catalog: UCAC4 Catalogue (Zacharias + , 2012). VizieR Online Data Catalog, page I/322 A (2012).
52. van Belle, G. T. Predicting Stellar Angular Sizes. *Pub. Astron. So. Pacific* **111**, 1515–1523 (1999).

Acknowledgements

B.J.H. acknowledges funding through NASA SSO #80NSSC20K0674. Part of this work was supported by the Spanish projects PID2020- 112789GB-I00 from AEI and Proyecto de Excelencia de la Junta de Andalucía PY20-01309. This research is partially based on observations collected at the Centro Astronómico Hispano-Alemán (CAHA) at Calar Alto, operated jointly by Junta de Andalucía and Consejo Superior de Investigaciones Científicas (IAA-CSIC). We acknowledge financial support from the Severo Ochoa grant CEX2021-001131-S funded by MCIN/AEI/ 10.13039/501100011033. P.S.-S. acknowledges financial support from the Spanish I + D + i project PID2022-139555NB-I00 funded by MCIN/AEI/10.13039/501100011033. This article is partly based on observations made in the Observatorio de Canarias of IAC with the Liverpool Telescope operated on the island of La Palma by the Liverpool JMU in the Observatorio del Roque de los Muchachos. Funding for the DPAC has been properly brightside by national institutions, in particular the institutions participating in the Gaia Multilateral Agreement. TRAPPIST is funded by the Belgian Fund for Scientific Research (FNRS) under the grant PDR T.0120.21. Michael Gillon is the FNRS Research Director and Emmanuel Jehin is a FNRS Senior Research Associate. J.d.W. and MIT gratefully acknowledge financial support from the Heising-Simons Foundation, Dr. and Mrs. Colin Masson and Dr. Peter A. Gilman for Artemis, the first telescope of the SPECULOOS network situated in Tenerife, Spain. Based on observations obtained at the Dominion Astrophysical Observatory, Herzberg Astronomy and Astrophysics Research Centre, National Research Council of Canada. This study was partly financed by the National Institute of Science and Technology of the e-Universe project (INCT do e-Universo, CNPq grant 465376/2014-2). This study was financed in part by CAPES – Finance Code 001. The authors acknowledge the respective CNPq grants: F.B.R. 316604/2023-2; B.E.M. 150612/2020-6; R.V.M. 307368/2021-1; M.A. 427700/2018-3, 310683/2017-3, 473002/2013-2; J.I.B.C. 305917/2019-6, 306691/2022-1 (CNPq) and 201.681/2019 (FAPERJ). This study was based in part on observations made at the Pico dos Dias Observatory, managed by the Laboratório Nacional de Astrofísica (LNA), Itajubá-MG, Brazil. Partially based on observations made with the Tx40 telescope at the Observatorio Astrofísico de Javalambre in Teruel, a Spanish Infraestructura Cientifico-Técnica Singular (ICTS) owned, managed and operated by the Centro de Estudios de Física del Cosmos de Aragón (CEFCA). Tx40 is funded with the Fondos de Inversiones de Teruel (FITE). C.K and A.P. acknowledge the K-138962 grant, and the TKP2021-NKTA-64 excellence grant of the National Research, Development and Innovation Office (NKFIH, Hungary).

Author contributions

E. Fernández-Valenzuela planned the main campaigns, participated in the observations, obtained and analyzed data, interpreted the data and wrote the paper. J.L. Ortiz planned the first campaign, analyzed data for the prediction, and made the prediction, and help with the interpretation of the data. B. Holler helped planning the main campaign, participated in the observations, obtained and analyzed data, and help with the interpretation of the data and writing the paper. F. L. Rommel helped analyzing data, interpreting the data and writing the paper. M. Vara-Lubiano produced the code for the three-dimensional shape and helped with the interpretation of the data. N. Morales helped planning the first campaign, analyzed data for the prediction, and obtained and analyzed data. F. Vachier and J. Desmars helped with the prediction analysis. All other authors participated in the planning of the campaign and/or performing observations and providing data and/or participated in the interpretations. All authors were given the opportunity to review the results and comment on the manuscript.

Competing interests

The authors declare no competing interests.

Additional information

Supplementary information The online version contains supplementary material available at https://doi.org/10.1038/s41467-025-65749-1.

Correspondence and requests for materials should be addressed to Estela Fernández-Valenzuela or Jose Luis Ortiz.

Peer review information *Nature Communications* thanks Qing-Yu Peng, and the other, anonymous, reviewers for their contribution to the peer review of this work. A peer review file is available.

Estela Fernández-Valenzuela[1] ✉, Jose Luis Ortiz[2] ✉, Bryan J. Holler[3], Bruno Sicardy[4], Flavia L. Rommel[1,5,6], Mónica Vara-Lubiano[2], Nicolas Morales[2], Frederic Vachier[7], Josselin Desmars[7,8], Mike Kretlow[2], Roberto Vieira-Martins[5,6], Emmanuel Jehin[9], Marin Ferrais[1], Pablo Santos-Sanz[2], Zafar Rustamkulov[10], Alexander de la Vega[11], Elizabeth Warner[12], Zouhair Benkhaldoun[13], Roxanne Kamin[14], Al Ryan[14], Bernie Earls[14], Dennis Conti[15], Julien de Wit[16], Artem Burdanov[16], Richard Francini[15,17], Philip Langill[18], Ruben Morales[18], Wesley Fraser[19,20], Csaba Kiss[21], András Pál[21,22,23], Damya Souami[4,24,25,26], Jean Lecacheux[4], Felipe Braga-Ribas[6,27], René Duffard[2], Alvaro Alvarez-Candal[2,28], Gustavo Benedetti-Rossi[4,6,29], Bruno Morgado[6,30], Julio I. B. Camargo[5,6], Altair Ramos Gomes Júnior[6,31], Marcelo Assafin[6,30], Djounai Baba Aissa[32], Zaki Grigahcene[32], Marc W. Buie[33], Javier Licandro[34], Miguel R. Alarcon[34], Miquel Serra-Ricart[34], Alberto Castro-Tirado[2], Emilio Jesus Fernandez-Garcia[2], Ramón Iglesias-Marzoa[35], Francisco J. Galindo-Guil[35], Hugo González[37], Rui Gonçalves[36], Adam Rengstorf[38], Randy Flynn[39], Aart Olsen[40], Bill Hanna[40], Jason Barnes[41], Joseph A. A'Hearn[41], Steven M. Kreyche[41], William J. Miller[41], Lillian E. Mortensen[41], Thomas C. Gibson[41], Gary Walker[42], Gerogia Stolle-McAllister[42], Gregory A. Feiden[43], Joseph Froetschel[43], Suzanne Steel[43], Destin Encardes[43], R. Scott Fisher[44], Alton Luken[44], Eric Holcomb[44], Daniel Caton[45], Bob Dunford[40] & Dmitry Monin[19]

[1]Florida Space Institute (University of Central Florida), 12354 Research Parkway, Partnership 1, Orlando, FL 32826, USA. [2]Instituto de Astrofísica de Andalucía - CSIC, Glorieta de la Astronomía S/N, 18008 Granada, Spain. [3]Space Telescope Science Institute, Steven Muller Building, 3700 San Martin Drive Baltimore, MD, 21218 Baltimore, MD, USA. [4]LESIA, Observatoire de Paris, PSL Research University, CNRS, Sorbonne Université, Université Paris Cité, 5 place Jules Janssen, 92195 Meudon, France. [5]Observatório Nacional, Ministério de Ciência, Tecnologia e Inovação, R. General José Cristino, 77, CEP 20921-400, Rio de Janeiro, RJ, Brazil. [6]Laboratório Interinstitucional de e-Astronomia - LIneA, Av. Pastor Martin Luther King Jr 126, CEP 20765-000, Rio de Janeiro, RJ, Brazil. [7]Institut de mécanique céleste et de calcul des éphémérides, University of Paris, 77, Avenue Denfert-Rochereau, 75014 Paris, France. [8]Institut Polytechnique des Sciences Avancées IPSA, 63 boulevard de Brandebourg, 94200 Ivry-sur-Seine, France. [9]Space Sciences, Technologies and Astrophysics Research (STAR) Institute, Université de Liège, Allée du 6 Août 19 C, B- 4000 Liège, Belgium. [10]Department of Earth and Planetary Science, Johns Hopkins University, 301 Olin Hall, 3400 N. Charles Street, Baltimore, MD 21218, USA. [11]Department of Physics and Astronomy, Johns Hopkins University, 3400 N. Charles Street, Baltimore, MD 21218, USA. [12]Department of Astronomy, University of Maryland, College Park, College Park, MD 20742, USA. [13]Oukaimeden Observatory, Cadi Ayyad University, Av Abdelkrim Khattabi, B.P. 511 – 40000, Marrakech, Morocco. [14]Ryan Observatory, Muddy Run, Bethesda Church Road West Holtwood, Holtwood PA 17532, USA. [15]American Association of Variable Star Observers, Annapolis, MD, USA. [16]Department of Earth, Atmospheric and Planetary Scienec (EAPS), Massachusetts Av Bldg 54, Cambridge, MA, USA. [17]Astronomical League and American Association of Variable Star Observers, 9201 Ward Parkway Suite 100, Kansas City, MO 64114, USA. [18]Department of Physics and Astronomy, University of Calgary, 2500 University Drive NW, Calgary, Alberta, Canada. [19]National Research Council, Herzberg Astrononomy and Astrophysics Research Centre, 5071 West Saanich Road, Victoria, BC, Canada. [20]Department of Physics and Astronomy, University of Victoria, Elliott Building, 3800 Finnerty Road, Victoria, BC V8P 5C2, Canada. [21]Konkoly Observatory, HUN-REN, Research Centre for Astronomy and Earth Sciences, Hungarian Academy of Sciences, Konkoly Thege 15-17, H-1121 Budapest, Hungary. [22]CSFK, MTA Centre of Excellence, BudapestKonkoly Thege 15-17, H-1121, Hungary. [23]ELTE Eötvös Loránd University, Institute of Physics and Astronomy, Pázmány Péter sétány 1/A, H-1171 Budapest, Hungary. [24]Departments of Astronomy and of Earth and Planetary Science, University of California, 501 Campbell Hall, Berkeley, CA 94720, USA. [25]naXys, University of Namur, 8 Rempart de la Vierge, Namur B-5000, Belgium. [26]Observatoire de la Côte d'Azur, Université Côte d'Azur, CRNS, Laboratoire Lagrange, Bd de l'Observatoire, CS 34229, 06304 Nice Cedex 4, France. [27]Federal University of Technology - Paran\'a, PPGFA/UTFPR-Curitiba, Av. Sete de Stembro 3165, 80230-901 Curitiba, PR, Brazil. [28]Instituto de Física Aplicada a las Ciencias y las Tecnologías, Universidad de Alicante, San Vicent del Raspeig, 03080 Alicante, Spain. [29]Grupo de Dinámica Orbital e Planetologia, UNESP – São Paulo State University, Av. Dr. Ariberto Pereira da Cunha, 333 - Pedregulho, Guaratinguetá SP 12516-410, Brazil. [30]Observatório do Valongo, Universidade Federal do Rio de Janeiro, Ladeira Pedro Antônio 43, CEP 20.080-090, Rio de Janeiro, RJ, Brazil. [31]Universidade Federal de Uberlândia (UFU), Instituto de Física, Av. Joñao Naves de Ávila 2121, Barrio Santa Mônica, Uberlândia, Brazil. [32]Center of Research in Astronomy, Astrophysics and Geophysics, CRAAG, bp – 63 Rte de l'Observatoire, Bouzareah Bouzareah, Algeria. [33]Southwest Research Institute, 1050 Walnut St 300, Boulder, CO 80302, USA. [34]Instituto de Astrofísica de Canarias, C. Vía Láctea, s/n, 38205 San Cristóbal de La Laguna, Santa Cruz de Tenerife, Spain. [35]Observatorio Astrofísico de Javalambre (OAJ), Centro de estudios de física del cosmos de Aragón (ceFca), Pl San Juán 1, 44001 Teruel, Spain. [36]Plan Occult, Tomar, Portugal. [37]Observatorio de Forcarei FC3 Fundación Ceo, Ciencia e Cultura, Edif. CC. Experimentais Campus Lagoas-Marcosende, 36310 Vigo, Spain. [38]Department of Chemistry and Physics, Purdue University Northwest, Hammond Campus 2200 169th St, Hammond, IN 46323, USA. [39]Squirrel Valley Observatory, 3870 River Rd, Columbus, NC 28722-6767, USA. [40]International Occultation Timing Association (IOTA), 16348 E Glenbrook Blvd, Fountain Hills, AZ 85268-2206, USA. [41]Department of Physics, University of Idaho, 875 Perimeter Dr, Moscow, ID 83844, USA. [42]Loines Observatory, Maria Mitchell Association, Nantucket's Science Center, 2 Vestal Street, Nantucket, MA 02554, USA. [43]Department of Physics, University of North Georgia, 82 College Cir, Dahlonega, GA 30597, USA. [44]University of Oregon, Deptartment of Physics, 1371 E 13th Ave, Eugene, OR 97403, USA. [45]Department of Physics and Astronomy, Appalachian State University, 231 Garwood Hall 525 Rivers Street Boone, Boone, NC 28608-2106, USA. ✉e-mail: estela@ucf.edu; ortiz@iaa.edu